BioMACROMOLECULES

pubs.acs.org/Biomac Article

Control of Peptide Amphiphile Supramolecular Nanostructures by Isosteric Replacements

Huihua Xing, Stacey M. Chin, Venkata Reddy Udumula, Krishnaiah Maddeboina, Nathalia Rodrigues de Almeida, Cristián Huck-Iriart, Agustín S. Picco, Sieun Ruth Lee, Gervasio Zaldivar, Kelsey A. Jackson, Mario Tagliazucchi, Samuel I. Stupp, and Martin Conda-Sheridan*

Cite This: https://doi.org/10.1021/acs.biomac.1c00379 Read Online

ACCESS | Metrics & More | Article Recommendations | Supporting Information

ABSTRACT: Supramolecular nanostructures with tunable properties can have applications in medicine, pharmacy, and biotechnology. In this work, we show that the self-assembly behavior of peptide amphiphiles (PAs) can be effectively tuned by replacing the carboxylic acids exposed to the aqueous media with isosteres, functionalities that share key physical or chemical properties with another chemical group. Transmission electron microscopy, atomic force microscopy, and small-angle X-ray scattering studies indicated that the nanostructure's morphologies are responsive to the ionization states of the side chains, which are related to their pK_a values. Circular dichroism studies revealed the effect of the isosteres on the internal arrangement of the nanostructures. The interactions between diverse surfaces and the nanostructures and the effect of salt concentration and temperature were assessed to further understand the properties of these self-assembled systems. These results indicate that isosteric replacements allow the pH control of supramolecular morphology by manipulating the pK_a of the charged groups located on the nanostructure's surface. Theoretical studies were performed to understand the morphological transitions that the nanostructures underwent in response to pH changes, suggesting that the transitions result from alterations in the Coulomb forces between PA molecules. This work provides a strategy for designing biomaterials that can maintain or change behaviors based on the pH differences found within cells and tissues.

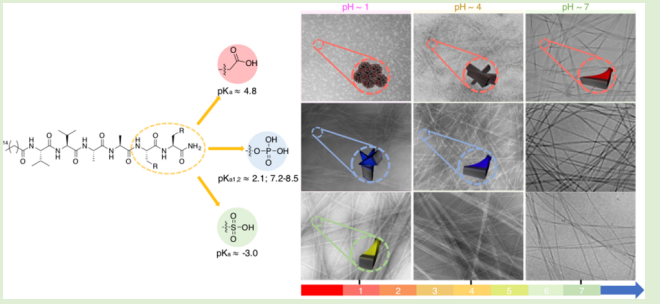

1. INTRODUCTION

The self-assembly process consists of the spontaneous organization of small building blocks into highly ordered supramolecular structures.[1−3] Among the reported self-assembling molecules, peptide amphiphiles (PAs) have become particularly attractive due to their potential therapeutic applications, including drug and protein delivery,[4−6] regenerative medicine,[1,7−9] and nanodrugs to treat cancer and bacterial infections.[10−12] Two decades ago, the Stupp laboratory developed a class of PAs that assemble into high-aspect ratio nanofilaments.[13] These PA molecules are composed of a hydrophobic alkyl tail connected to a peptide sequence that can form β-sheet interactions and a charged portion to enhance water solubility. These PA nanostructures have also been designed to display a bioactive epitope for targeting or cell signaling.[13−15]

To control these supramolecular assemblies, it is necessary to understand how the PAs respond to pH, salt concentration, solvent, or heat changes. Seminal studies from the groups of Stupp,[16,17] Meijer,[18] Goldberger,[19,20] and Guler[21,22] have highlighted the effects of pH, media, and processing on the supramolecular architecture. Meanwhile, Shen and co-workers[23] have shown that a decrease in electrostatic repulsions shifts the morphology from micelles to fibers. Furthermore, Zaldivar et al.[24] combined experiments with a molecular theory (herein termed as MOLT) to demonstrate that controlling the pH of the solution triggers a micelle−fiber−lamella transition.

Thus, to enhance the function *in operando*, it is necessary to understand the effect of external conditions on the characteristics of a supramolecular system. This information can then be used to enhance the stability of the nanostructure against an external stimulus (pH, temperature, and ionic strength) or to create nanostructures that respond to environmental cues (i.e., supramolecular transition at a desired location).[25−27] An unexplored strategy to achieve such control is the use of isosteric replacements. Isosteres are used in medicinal chemistry to modulate physicochemical characteristics such as size, electronegativity, and topology,[28] solubility, and metabolism.[29] In this work, we have merged medicinal chemistry with materials

Received: March 23, 2021
Revised: July 8, 2021

ACS Publications © XXXX American Chemical Society

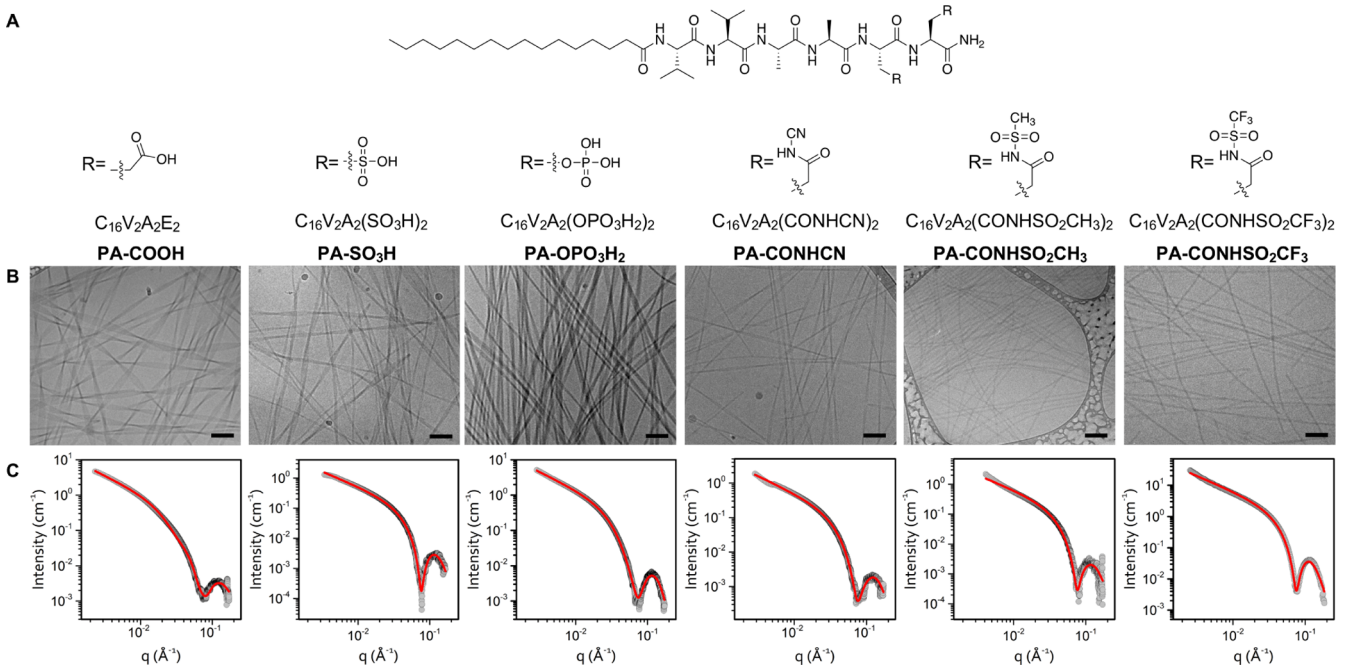

Figure 1. (A) Chemical structures of the PAs studied in this work. The chemical structure of the six different R groups and the nomenclature used for the derived PAs are shown: $C_{16}V_2A_2E_2$ (**PA-COOH**), $C_{16}V_2A_2(SO_3H)_2$ (**PA-SO$_3$H**), $C_{16}V_2A_2(OPO_3H_2)_2$ (**PA-OPO$_3$H$_2$**), $C_{16}V_2A_2(CONHCN)_2$ (**PA-CONHCN**), $C_{16}V_2A_2(CONHSO_2CH_3)_2$ (**PA-CONHSO$_2$CH$_3$**), and $C_{16}V_2A_2(CONHSO_2CF_3)_2$ (**PA-CONHSO$_2$CF$_3$**). (B) Cryo-TEM images of PAs. Black lines in the lower right corner of cryo-TEM images represent the scale bars (100 nm). Original figures are shown in Figure S3. (C) SAXS curves of PAs self-assembled in water. The gray points represent the raw data, and the red curves show the best fit obtained by a model of an infinite ribbon with a rectangular core−shell cross-section (see text and the Supporting Information). All samples were prepared in Milli-Q water, at 1 mg/mL, and the pH was adjusted to 7.4.

science to develop novel self-assembling materials. We hypothesized that the pK_a values of solvent-exposed charged groups should influence the supramolecular morphology and stability in response to pH. We synthesized six PA molecules with anionic headgroups of various pK_a values to assess their self-assembly properties under diverse conditions. All PA molecules had the same hydrophobic segment (C_{16}) covalently conjugated to an amino acid sequence (V_2A_2), which has been previously shown to promote the formation of elongated nanostructures at physiological pH.[23] Through detailed experimental characterization and theoretical modeling of these six anionic PAs, we systematically investigated how groups with different pK_a values respond to the environment (i.e., pH, salt concentration, surface charge) and the effect they exert on the supramolecular behavior.

2. EXPERIMENTAL SECTION

Materials. Solvents and coupling agents were purchased from Fisher Chemical. Fmoc-amino acids and coupling reagents were obtained from P3Bio (Louisville, KY). Fmoc-Rink Amide AM resin (0.61 mmol/g) was purchased from CreoSaulus (Louisville, KY). Fmoc-L-cysteic acid and Fmoc-L-Ser(PO_3BzlH)-OH were purchased from Combi-Blocks. Buffers were prepared as shown in Table S1.

Synthesis and Characterization of PAs. Isosteric amino acids were synthesized (Scheme S1) and characterized, as described in the Supporting Information (Experimental Procedures section, Figures S1−S4). The PAs were prepared using standard Fmoc solid-phase peptide synthesis (SPPS) on a 0.3 mmol scale on Fmoc-Rink Amide AM resin and using HBTU/DIPEA (or DIC/DIPEA) as coupling reagents, as published or as indicated in the Supporting Information.[12] The PAs were purified and characterized as reported (Figures S6−S11).[12,24] The purities of the fractions containing the desired PAs were confirmed by analytical HPLC (Agilent) using a C_{18} Kinetex column [5 μm XB-C18 100 Å, 250 × 4.6 mm] (Phenomenex). The UV detector was set at 220 nm wavelength, and elution was achieved with a linear gradient of ACN/H_2O (both containing 0.1% ammonium hydroxide) from 5 to 95% for 25 min. The fractions with purity >95% were combined, the organic solvent was removed under vacuum, the pH was adjusted to 7.0 (0.1 M HCl or NaOH), and the solution was lyophilized (FreeZone, Labconco).

Self-Assembly. Lyophilized PAs were dissolved in water (2 mg/mL), annealed at 80 °C for 2 h, and cooled to room temperature. Samples were diluted with the desired media to achieve a final concentration of 1 mg/mL and aged for 24 h before testing. The final pH was measured using a pH meter. Additional details can be found in Scheme S2.

Transmission Electron Microscopy. The PAs in different pH buffers (1 mg/mL) were prepared and aged for 24 h. Approximately, 6 μL of the sample was applied into a copper grid and allowed to absorb for 5 min, covered with a folded piece of filter paper. The excess PA was removed by touching the edge of the grid with a clean piece of filter paper. Then, 6 μL of the negative stain (NanoVan) was added, and the system was incubated for 30 s. The excess stain was blotted off as before, and the sample was incubated for 5 min. PAs were visualized with a FEI Tecnai G2 Spirit transmission electron microscope (120 kV). Images were acquired using an AMT digital imaging system.

Cryogenic Transmission Electron Microscopy. Copper grids (300-mesh) with a lacey carbon support (Electron Microscopy Sciences) were glow-discharged for 15 s using a PELCO easiGlow Glow Discharge Cleaning System (Ted Pella) and used immediately. The samples were prepared via plunge freezing using a Vitrobot Mark IV (FEI) vitrification robot at room temperature and 90−100% humidity. The annealed PA solution (7 μL, 1 mg/mL) was placed on the copper grid, blotted, and plunge-frozen into liquid ethane. Samples were transferred immediately into a liquid nitrogen bath and held until imaging. During imaging, samples were moved into a Gatan 626 cryo-holder through a cryo-transfer stage. The study was performed using a JEOL 1230 transmission electron microscope working at 100 kV accelerating voltage, and the images were obtained with a Gatan 831 CCD camera.

https://doi.org/10.1021/acs.biomac.1c00379
Biomacromolecules XXXX, XXX, XXX−XXX

Table 1. Width of PAs Measured by SAXS, AFM, and Cryo-TEM

PA	cryo-TEM (nm)	SAXS (nm)	AFM (nm)	
			width	height
PA-COOH	31.4 ± 8.6	25.7 ± 0.4	32.0 ± 4.6	6.8 ± 1.3
PA-SO_3H	15.8 ± 5.4	12.7 ± 0.2	15.5 ± 0.9	6.1 ± 0.6
PA-OPO_3H_2	17.5 ± 4.1	18.6 ± 0.6	24.9 ± 4.1	6.4 ± 0.4
PA-CONHCN	15.3 ± 2.4	15.3 ± 0.1	17.6 ± 0.2	6.2 ± 0.6
PA-$CONHSO_2CH_3$	9.9 ± 1.4	14.6 ± 0.3	13.5 ± 4.0	5.5 ± 0.2
PA-$CONHSO_2CF_3$	11.1 ± 1.6	12.0 ± 1.8	12.8 ± 0.8	4.3 ± 0.5

Experimental details for small-angle X-ray scattering (SAXS), circular dichroism (CD), atomic force microscopy (AFM), in situ AFM, and infrared (IR) spectroscopy can be found in the Supporting Information section.

3. RESULTS AND DISCUSSION

PA Design and Characterization. Our objective was to assess the effect of carboxylic acid isosteres on supramolecular self-assembly. We prepared six PAs,[12,30] composed of an alkyl chain (C_{16}), a β-sheet promoting sequence (V_2A_2), and a hydrophilic headgroup (R) (Figure 1A). The charged group, R, was either a carboxylic acid (**PA-COOH**, $pK_a \approx 4.8$)[31] or one of its isosteres: sulfonic acid (**PA-SO_3H**, reported pK_a ranges from −1 to −6),[32−34] phosphoric acid (**PA-OPO_3H_2**, $pK_{a1} \approx 2.1$, $pK_{a2} \approx 7.2$−8.5),[28,35] cyanamide (**PA-CONHCN**, $pK_a = 3.8$),[36] methyl sulfonamide (**PA-$CONHSO_2CH_3$**, $pK_a = 4.94$),[28] or trifluoromethyl sulfonamide (**PA-$CONHSO_2CF_3$**, $pK_a = 3.04$ calculated with MarvinSketch[37]).

The PAs were dissolved in water (pH adjusted to 7.4), and their supramolecular shape was studied by cryogenic transmission electron microscopy (cryo-TEM), AFM, and small-angle X-ray scattering (SAXS). Cryo-TEM shows that **PA-COOH**, **PA-SO_3H**, **PA-OPO_3H_2**, and **PA-CONHCN** formed elongated twisted ribbons (Figures 1B and S12). **PA-COOH** exhibited the widest ribbons (width ∼31 nm), while narrower ones were observed for **PA-SO_3H**, **PA-OPO_3H_2**, and **PA-CONHCN** (width 15−17 nm). On the other hand, **PA-$CONHSO_2CH_3$** and **PA-$CONHSO_2CF_3$** assembled into thin ribbons (or nanofibers), with diameters of ∼11 nm. The difference in width seems to be related to the bulkiness of the side chain (except for **PA-SO_3H**, Table S2). AFM also showed the presence of elongated nanostructures (Figure S13).

The SAXS curves of all the PAs presented low-angle (Guinier) regions with slopes between −1 and −1.5, which is a key signature of high-aspect ratio objects.[38,39] The SAXS data were modeled using a core−shell ribbon model (details can be found in the Supporting Information). The analysis indicates that **PA-COOH** forms the widest nanostructures (∼26 nm), while the other PAs exhibited lower values (13−19 nm). The results are summarized in Tables 1 and S2 and S3. The height of the nanostructures was similar in SAXS and AFM, ranging from 4.3 to 7.8 nm.

pH Effect on the Morphology and Secondary Structure. Next, we studied the effect of pH (1, 4, 6, and 9) on self-assembly by TEM. At pH = 1, **PA-COOH** formed amorphous aggregates that may be attributed to the carboxylic acid pK_a (∼4.8), which makes the PA heads neutral at pH = 1 (pH 1: ∼0.016% ionization). The decrease in the electrostatic repulsion between PA molecules leads to the formation of aggregates. At pH = 4 (∼15.85% ionization), **PA-COOH** formed a mixture of short ribbons and micelles, while twisted ribbons were seen at pH 6 and 9. **PA-SO_3H** formed elongated nanostructures at all pH values (Figure 2B). This can be explained by considering the pK_a of the sulfonate group (<0), which enables the isostere to be fully deprotonated at all pH values investigated. **PA-OPO_3H_2** also showed short fiber-like structures at pH = 1 but high-aspect ratio nanostructures at pH = 4, presumably because the headgroup is negatively charged at the latter pH ($pK_{a1} \sim 2.1$). At pH = 6, twisted ribbons are present. Furthermore, we observed that **PA-OPO_3H_2** displayed some shorter ribbons at pH 9. This may be related to the partial deprotonation of the second hydroxyl group on the phosphoric acid ($pK_{a2} \sim 7.2$), which could increase Coulomb repulsions that disrupt the ribbons. To confirm this observation, we performed TEM at pH 11 and 12 (Figure S14). We observed long and short elongated structures, which further suggests that the increased repulsion caused by the second deprotonation prevents the formation of long ribbons. **PA-CONHCN**, **PA-$CONHSO_2CH_3$**, and **PA-$CONHSO_2CF_3$** also show shorter structures at pH = 1. This is more evident in **PA-$CONHSO_2CH_3$**, which possesses a pK_a of ∼4.9. At pH 4, 6, and 9, these PAs formed twisted ribbons or fibers, although in some cases, it was difficult to detect twisting in the nanostructures.

We performed in situ AFM on four of the PAs to understand if a pre-formed morphology will respond to changes in pH. As can be seen in Figure S15, **PA-COOH**, **PA-SO_3H**, **PA-OPO_3H_2**, and **PA-CONHCN** all formed fibers at pH 6, consistent with the cryo-TEM data (although some short fibers were also seen in this experiment). When the pH was lowered to 1, the PAs with $pK_a <$ pH changed shape, giving rise to short supramolecular structures. The observed results are consistent with those of pH 1 cryo-TEM.

Next, we studied **PA-COOH**, **PA-SO_3H**, and **PA-OPO_3H_2** using SAXS (Figure S16; pH 1, 6, and 9). We selected these three PAs because of their pK_a differences. At pH 1, **PA-COOH** and **PA-OPO_3H_2** showed Guinier regions with slopes around −2, a signature of flat assemblies (the cryo-TEM shows small structures). At pH 6, the slope of **PA-COOH** is around −2 (but not as pronounced as in the previous case), but for **PA-OPO_3H_2**, the slope is closer to −1 than −2. At pH = 9, both **PA-COOH** and **PA-OPO_3H_2** exhibited curves with slopes close to −1 in the low-angle region, indicating the formation of high-aspect ratio assemblies. On the other hand, **PA-SO_3H** exhibited a slope of −1 at all pH values, which is consistent with the unaltered long-ribbon morphology (Figure 2B). Thus, the pH studies by TEM and SAXS indicated that the lower the pK_a of the headgroup, the stronger its ability to prevent supramolecular transitions.

In addition, we studied how pH can alter the secondary structure of the assemblies (Figure 2, right-side column). The CD spectra of elongated PA nanostructures typically present β-sheet positive bands at ∼200 nm and negative ones around 220 nm.[13,16] The changes in the secondary structure could indicate an internal rearrangement, which can be associated with

https://doi.org/10.1021/acs.biomac.1c00379
Biomacromolecules XXXX, XXX, XXX−XXX

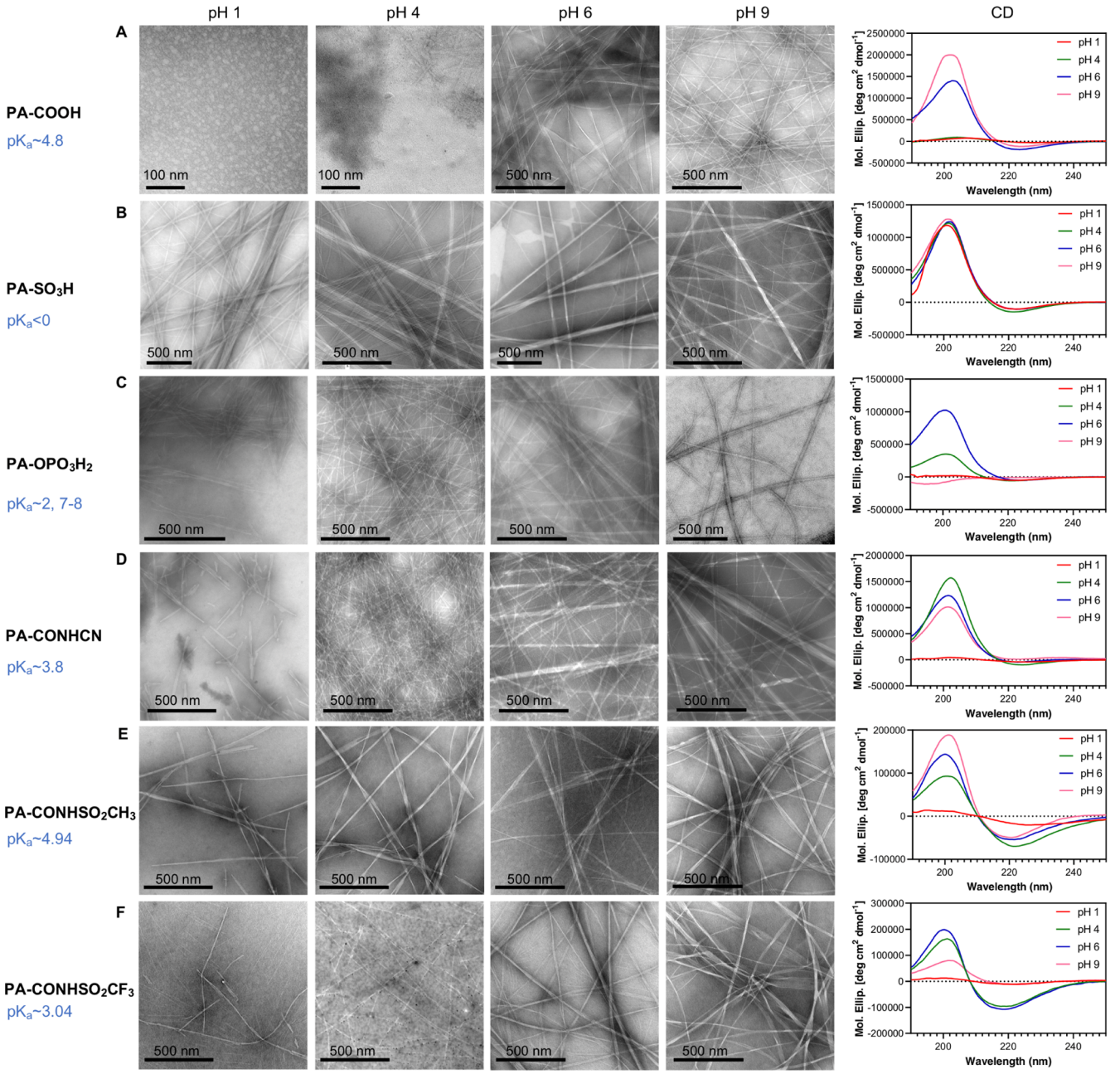

Figure 2. TEM images (first four columns) and CD spectra (right-hand column) of (A) **PA-COOH**, (B) **PA-SO_3H**, (C) **PA-OPO_3H_2**, (D) **PA-$CONHSO_2CH_3$**, (E) **PA-$CONHSO_2CF_3$**, and (F) **PA-CONHCN** at pH = 1, 4, 6, and 9 from left to right. Samples were prepared at 1 mg/mL and aged for 24 h.

morphological and/or assembly−disassembly transitions.[18,40] **PA-COOH** lacked a secondary structure at pH 1 and 4 but exhibited β-sheets peaks at pH 6 and 9. This correlates with TEM and SAXS, where irregular aggregates are seen at pH 1 and 4, while twisted ribbons are present at pH 6 and 9. Supporting what was observed by TEM and SAXS, the CD spectra of **PA-SO_3H** remained almost unaltered from pH 1 to 9. **PA-OPO_3H_2** presented β-sheet peaks at pH 4 and 6 (long ribbons by TEM) and no clear CD features at pH 1. At pH 9, the CD spectra of **PA-OPO_3H_2** were consistent with a random coil (negative peak below 200 nm).[18] As previously described, **PA-OPO_3H_2** exhibited shorter ribbons due to the strong intermolecular repulsions at high pH. The remaining PAs, **PA-CONHCN**, **PA-$CONHSO_2CH_3$**, and **PA-$CONHSO_2CF_3$**, exhibited poorly defined β-sheet peaks at pH 1 but well-defined peaks at higher pH (elongated nanostructures by TEM). Notably, these three PAs formed some fiber-like structures at the lowest pH even in the absence of β-sheet signature peaks. Furthermore, the maxima of the three PAs did not increase with pH, indicating that other factors, besides pK_a, affect the internal arrangement. We also performed infrared (IR) spectroscopy studies on the PAs, as detailed in Figures S17 and S18. We were able to observe peaks that can be ascribed to β-sheet signals.

As described, some PAs form aggregates when pK_a < pH. This can be caused by (1) the collapse of the nanostructures as they lose colloidal stability at low pH or (2) by the agglomeration of the molecules into disordered aggregates due to reduced water solubility. The first hypothesis is supported by a theoretical

https://doi.org/10.1021/acs.biomac.1c00379
Biomacromolecules XXXX, XXX, XXX−XXX

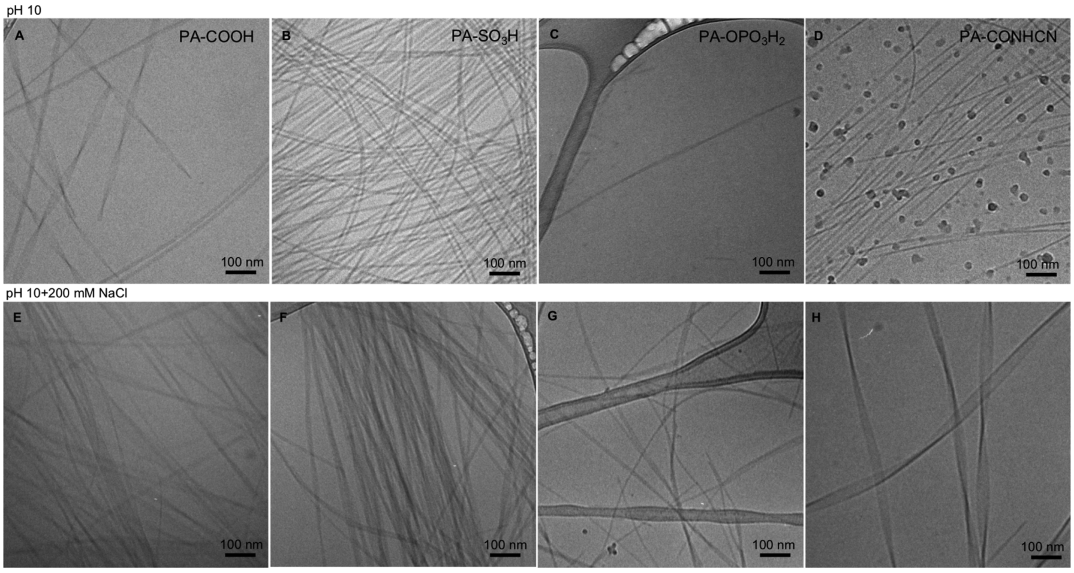

Figure 3. Cryo-TEM images of (A,E) **PA-COOH;** (B,F) **PA-SO_3H**; (C,G) **PA-OPO_3H_2**; and (D,H) **PA-CONHCN** at pH 10 (50 mM glycine−32 mM NaOH buffer; 1 mg/mL concentration) without and with NaCl (200 mM), respectively. Scale bar: 100 nm.

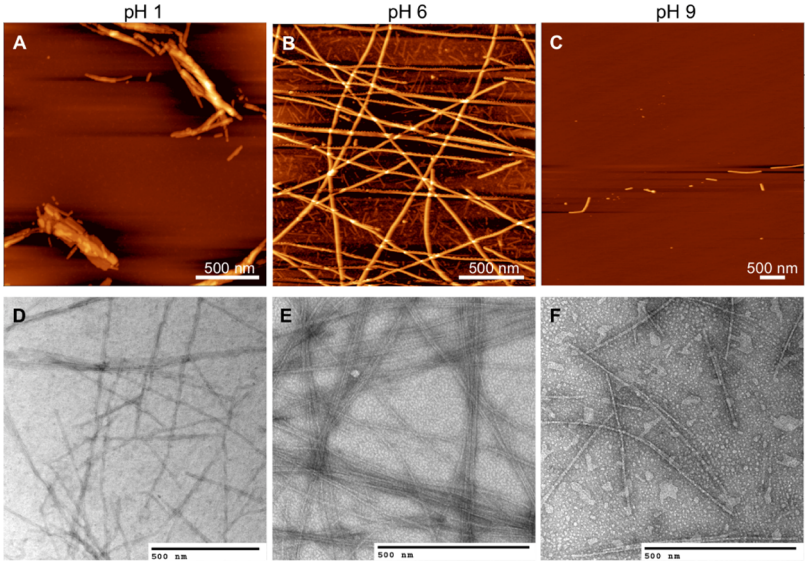

Figure 4. (A−C) AFM images and (D−F) TEM images (scale bar 500 nm) of **PA-OPO_3H_2** on the positively charged mica (top) or grid (bottom) at pH 1, 6, and 9, respectively.

model (see below) that predicts that PA nanostructures lose colloidal stability (i.e., aggregation is thermodynamically favored) at pH values similar to those where aggregates are observed in the TEM images (Figure 2). This is consistent with the fact that the nanostructures of **PA-COOH** at pH 4 and **PA-OPO_3H_2** at pH 1 seem to be composed of aggregated lamellar objects. Note that it is unlikely that the aggregates observed for **PA-COOH** at pH 1 are the result of a ribbon-to-micelle transition, since this transition takes place with increased PA charge (more repulsions).[24,41] As a general rule, it can be said that when pH > pK_a of the headgroups, β-sheet features are found by CD and elongated nanostructures are observed by TEM and AFM. In contrast, when pH < pK_a of the headgroups, there is a lack of secondary structure and aggregates are formed. Other factors, besides pK_a (i.e., hydrogen bonds provided by the side chains, bulkiness of the side chain, and hydrophobicity) may play a key role in the formation and structure of the supramolecular assemblies.

Effect of Charge Screening. We selected four of the PAs and studied if the ionic strength of the media affects the supramolecular morphology. The addition of NaCl (200 nM) to a pH 7 solution did not affect the shape of the nanostructures formed by **PA-COOH**, **PA-SO_3H**, and **PA-CONHCN** (Figure S19). However, **PA-OPO_3H_2** showed needle-like structures, slightly shorter than what was observed before (Figure S20). Next, we performed cryo-TEM and AFM at pH 10 without and with the addition of NaCl. As can be seen in Figures 3 and S21, the PAs maintained their elongated morphology. **PA-OPO_3H_2** still showed the presence of some shorter fibers, presumably due to electrostatic repulsions due to the deprotonated headgroups, but the addition of NaCl seemed to increase the length of the fibers. This can be rationalized by the fact that the negative charges may be more sensitive to the higher ionic content in the

https://doi.org/10.1021/acs.biomac.1c00379
Biomacromolecules XXXX, XXX, XXX−XXX

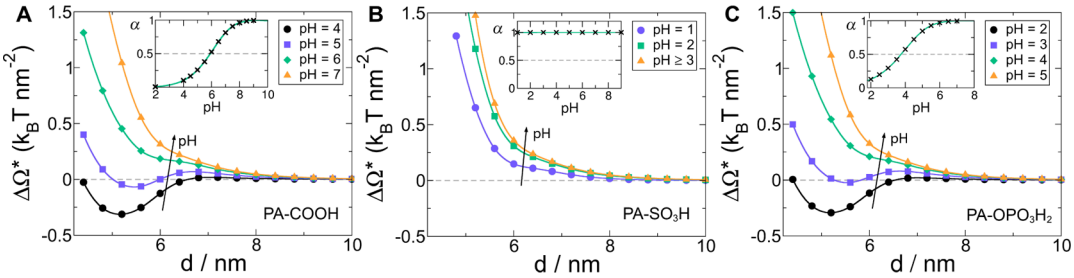

Figure 5. Free energy per unit of area, $\Delta\Omega^*$, of two ribbons of (A) **PA-COOH**, (B) **PA-SO_3H**, and (C) **PA-OPO_3H_2** as a function of the distance between them, d, at different pH values. $\Delta\Omega^*$ is defined with respect to the free energy of two infinitely separated ribbons. The insets show the fraction of carboxylate groups, sulfonate groups, and phosphonate groups that are deprotonated, α, as a function of pH. The salt concentration was set to 0.1 M in all calculations.

solution. The results described here indicated that in general, the salt concentration does not have a significant effect on the morphology of the nanostructures formed by the PA-isosteres under the tested conditions.[24]

Structural Studies on Charged Surfaces. Next, we decided to assess how a positively charged surface affects supramolecular morphology by altering the mica (used in AFM) and the grid (TEM) (details can be found in the Supporting Information). We studied **PA-COOH**, **PA-SO_3H**, and **PA-OPO_3H_2** due to their diverse pK_a values. We found that at pH 1, **PA-COOH** assembles into short ribbons (Figure S22) instead of aggregates (Figure 2A). This is possibly due to the electrostatic interactions with the cationic surfaces, which were not present before functionalization. At pH 6 and 9, we saw elongated nanostructures. **PA-SO_3H** provided elongated structures at all the pH values (Figure S23), also consistent with the earlier TEM study (Figure 2B), although at pH 9, we still observed some short, entangled ribbons by AFM. **PA-OPO_3H_2** presented shorter fibers (and perhaps some aggregates) at pH 1 and 9 (compare Figures 2C and 4) but elongated objects at pH 6. Altogether, the results of the study show that surface charge has a minimal effect on the supramolecular shape of the PAs.

Effect of Temperature. Then, we performed variable-temperature SAXS (25−90 °C, pH = 7.4) to evaluate the thermal stability of selected nanostructures (Figure S24). The stability rank was **PA-SO_3H** ∼ **PA-OPO_3H_2** < **PA-CONHCN** < **PA-COOH** (see the Supporting Information for details). Based on the results, we hypothesize that the stability is related to the width of the self-assembled structures (**PA-COOH** is the widest). A potential explanation is that thinner ribbons possess fewer molecules within its cross-section, which translates to less interactions (fewer hydrogen bonds), leading to a decrease in stability. An alternative explanation is related to the increased motion of water at higher temperatures. Higher temperature weakens hydrogen bonding[42,43] between the PAs and the water molecules leading to a decrease in charge screening. This increases the charge repulsion, causing a morphological transition. Since **PA-COOH** is the molecule with the least potential for hydrogen bonding in the headgroups, it may have fewer associated water molecules. This results in less charge screening and a less-noticeable temperature-induced change. **PA-SO_3H** and **PA-OPO_3H_2** should have a higher number of associated water molecules. The reduced charge screening, due to water movement, will increase the repulsive forces, promoting a morphological transition. Based on the NaCl experiments described earlier, we theorize that the thermal stability of the nanostructures is related to the cross-section of the PAs.

Molecular Theory of PA Aggregation. We used a MOLT approach to explain if the observed morphologies are the result of the competition between hydrophobic attractive interactions and a decrease in Coulomb repulsions (see Figure S25 and associated text for details). We hypothesized that at low pH, the ribbons "stick together" because the acidic groups of the PAs are protonated, making the Coulomb repulsions negligible. To test the hypothesis, we calculated the free energy of two approaching ribbons as a function of pH. The free energy estimation was done using our previously reported model,[24] which explicitly incorporates the molecular details of the PAs (molecular structure, conformations, volume and charge distribution, and inter- and intramolecular interactions) and the properties of the solution (pH and ionic strength). Figure 5A shows the free energy per unit area of two lamellar ribbons formed by **PA-COOH**, $\Delta\Omega^*$, as a function of the distance between them, d. The free energy is defined with respect to that of two lamellas infinitely separated, $\Delta\Omega^* = \Omega^*(d) - \Omega^*(d \to \infty)$. For pH ≥ 6, the free energy increases as the ribbons approach, indicating that the formation of a superaggregate of ribbons is unstable. For pH ≤ 5, the free energy reaches a global minimum at $d \sim 5.5$ nm, which indicates that the aggregated state is stable.

The model predicts a transition from isolated ribbons to ribbon aggregates at pH ∼ 5. We speculate that ribbon aggregation can lead to amorphous aggregates or precipitation. To support this interpretation, we show in the inset of Figure 5A our prediction for the fraction of charged carboxylate groups, $\alpha = [PACOO^-]/([PACOOH] + [PACOO^-])$, as a function of pH. The fraction was using the approach reported in our previous work.[24] At low pH, all carboxylate groups are uncharged ($\alpha \sim 0$, inset of Figure 5A), and the ribbons stick together due to hydrophobic attractions. An increase in pH increases the fraction of charged carboxylates (see α in the inset), and consequently, the Coulomb repulsions disfavor the PA nanostructures closely approaching each other. At pH ∼ 6 ($\alpha \sim 0.5$), the repulsions are high enough to balance the hydrophobic attractions, and the aggregate becomes "unstable". Note that the pK_a is higher within the individual elongated ribbons (apparent p$K_a \sim 6$, see the inset of Figure 5A) than in bulk solution (p$K_a \sim 4.8$). This pK_a shift is due to a charge regulation effect that has been reported in the literature.[24]

All PAs showed the same behavior as **PA-COOH** except for **PA-SO_3H**, which possesses pK_a < pH (Figures 5B,C and S26D−F). In general, the PAs are predicted to transition from ribbons to aggregates (or micelles) with decreasing pH. The pH at which this transition occurs depends on the apparent pK_a of each PA; see inset plots in Figures 5 and S26. Note that the pK_a of all PAs experiences a shift due to the charge regulation effects explained

https://doi.org/10.1021/acs.biomac.1c00379
Biomacromolecules XXXX, XXX, XXX−XXX

above. The ribbon aggregates of **PA-SO_3H** are not favored for all pH values (Figure 5B) because pK_a < pH.[32] This ensures that all sulfonic groups are deprotonated, that is, $\alpha \sim 1$ for all pH (negative pK_a values will not affect our calculations), ensuring that the Coulomb repulsions dominate over the hydrophobic attractive interactions (preventing aggregation).

Structural Properties of the Twisted Ribbons. We have shown that **PA-COOH**, **PA-SO_3H**, and **PA-OPO_3H_2** self-assembled into twisted ribbons at pH > pK_a (Figure 2, **PA-CONHCN** also formed twisted ribbons, while the other two PAs formed thin ribbons or nanofibers). These structures possess characteristic width (W) and twisting pitch (P). Figure 6A

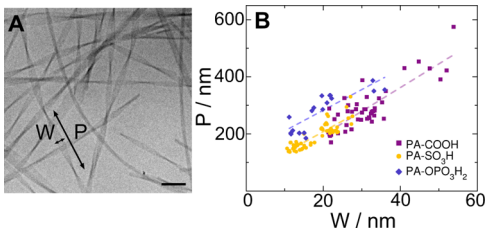

Figure 6. (A) Cryo-TEM images of **PA-COOH** in PBS buffer. Double arrows mark the width (W) and pitch (P) of the ribbons (scale bar 100 nm). (B) Twisting pitch (P) as a function of the width (W) of twisted ribbons formed by **PA-COOH**, **PA-SO_3H**, and **PA-OPO_3H_2** in PBS buffer.

shows the cryo-TEM of **PA-COOH**. The aggregates formed by these PAs present some polydispersity in both width and period, with values around 10−60 and 150−500 nm, respectively. Remarkably, these parameters are not independent of each other. Figure 6B shows P as a function of W for ribbons formed by **PA-COOH**, **PA-SO_3H**, and **PA-OPO_3H_2** in PBS buffer (pH = 7.4). P and W were measured from several cryo-TEM images using ImageJ software.[44] The plot suggests that there is an approximately linear correlation between P and W. This correlation has not been reported before for PAs, but it has been previously observed in related self-assembled systems.[45−47]

There is reasonable consensus in the literature that the twisting of self-assembled ribbons arises mainly from chiral interactions between the building blocks,[48,49] with a minor but not always negligible contribution from electrostatic interactions.[50−52] The degree of twisting is mainly defined by the competition between a chiral interaction that defines an optimal angle a_0 between two consecutive molecules and an elastic resistance. As a result, an equilibrium angle a^* ($a^* < a_0$) between consecutive molecules arises and propagates in one direction. In PAs, the chiral interactions are presumably influenced by the stereochemistry of the side chains, while the elastic resistance is due to the tail−tail hydrophobic attraction that is maximized in the untwisted ribbon. Recently, Zhang et al.[45] showed that the positive correlation between the period (P) and width (W) can be understood and quantitatively predicted by a mechanical model that considers such chiral interactions.

Helicoid-shaped ribbons are chiral nanostructures that have either right-handed or left-handed twisting. We used AFM to determine the direction of rotation of the ribbons (Figures S27 and S28). The analysis of AFM images supports the hypothesis of the chiral origin of the twisting for two reasons. First, all the ribbons formed by a given PA present the same chirality, which is expected if the twisting arises from the molecular chirality (we used only L-amino acids). Second, making isosteric replacements in the PA did not change the macromolecular chirality. This result suggests that the replacements do not significantly affect the packing of consecutive molecules due to peptide−peptide hydrogen bonds. This conclusion is valid for the PAs analyzed herein because their acidic groups have similar molecular volumes.

4. CONCLUSIONS

We have prepared PAs that contain the same hydrophobic tail and peptide core but possess different anionic groups (carboxylic acid, sulfonic acid, phosphoric acid, methyl sulfonamide, methyl sulfonamide, trifluoromethyl sulfonamide, and cyanamide) to investigate the effect of isosteric replacement (pK_a) on self-assembly. Our data indicate that the self-assembly behavior of PAs is dependent on the pK_a of the ionizable groups. Changes in the solution pH can trigger structural rearrangements at the supramolecular level. However, if the pK_a value is below the solution's pH, the supramolecular morphology will not change. Theoretical studies indicate that this morphological transition is related to changes in the Coulomb repulsions among self-assembled PA nanostructures. The aggregation of these nanostructures occurs when electrostatic repulsions are overcome by hydrophobic attractions. The study on the nanostructure's twisting property indicates that the isosteric replacement does not change the macromolecular chirality. The property of headgroups is found to influence the width and twisting of the assembled ribbons and the secondary structure. Moreover, the nanostructures' thermal stability is related to the morphology of assemblies and physicochemical characters of the headgroups. This information will be valuable to the development of supramolecular nanostructures with pH-responsive or pH- and thermal-resistant properties, thus expanding the potential applications of PA-based nanosystems. Potential future uses of this technology include nanocarriers for oral drug delivery and shape-changing nanostructures to achieve enhanced cell binding, fast clearance, or burst drug release. For example, since its shape is unaltered at low pH (such as the environment of the digestive system), **PA-SO_3H**-based nanostructures may be an intriguing option for oral delivery. Meanwhile, the other PAs could change their supramolecular structure in the intestine, pancreas, or duodenum (areas with different pH values), releasing drugs or exposing signaling ligands upon conformational changes.

■ ASSOCIATED CONTENT

Supporting Information

The Supporting Information is available free of charge at https://pubs.acs.org/doi/10.1021/acs.biomac.1c00379.

Protocol to prepare PA nanostructures; buffer preparation; SAXS model; schematic representation of SAXS; PA chemical structures; mass spectra; HPLC chromatograms; AFM micrographs for nanostructures; table of measurements of nanoparticles at pH 7.4 by cryo-TEM; table of parameters by SAXS; SAXS patterns at different pH values; nanostructure TEM micrographs at different pH and salt concentration values; AFM and TEM micrographs with a positively charged surface; and theoretical studies (PDF)

■ AUTHOR INFORMATION

Corresponding Author

Martin Conda-Sheridan − *College of Pharmacy, University of Nebraska Medical Center, Omaha, Nebraska 68105, United*

https://doi.org/10.1021/acs.biomac.1c00379
Biomacromolecules XXXX, XXX, XXX−XXX

States; orcid.org/0000-0002-3568-2545; Phone: +1 402-559-9361; Email: martin.condasheridan@unmc.edu

Authors

Huihua Xing − *College of Pharmacy, University of Nebraska Medical Center, Omaha, Nebraska 68105, United States*

Stacey M. Chin − *Department of Chemistry, Northwestern University, Evanston, Illinois 60208, United States;* orcid.org/0000-0002-2909-6080

Venkata Reddy Udumula − *College of Pharmacy, University of Nebraska Medical Center, Omaha, Nebraska 68105, United States;* orcid.org/0000-0002-7044-2029

Krishnaiah Maddeboina − *College of Pharmacy, University of Nebraska Medical Center, Omaha, Nebraska 68105, United States*

Nathalia Rodrigues de Almeida − *College of Pharmacy, University of Nebraska Medical Center, Omaha, Nebraska 68105, United States;* Present Address: College of Chemistry, University of Nebraska Omaha, 6001 Dodge Street, Omaha, NE 68182, United States; orcid.org/0000-0002-9552-1233

Cristián Huck-Iriart − *Laboratorio de Cristalografía Aplicada, Escuela de Ciencia y Tecnología, Universidad Nacional de General San Martín, B1650 San Martín, Buenos Aires, Argentina;* orcid.org/0000-0001-5734-2499

Agustín S. Picco − *Instituto de Investigaciones Fisicoquímicas Teóricas y Aplicadas, INIFTA-CONICET-UNLP, B1900 La Plata, Argentina*

Sieun Ruth Lee − *Department of Chemistry, Northwestern University, Evanston, Illinois 60208, United States*

Gervasio Zaldivar − *INQUIMAE-CONICET and DQIAQF, Universidad de Buenos Aires, Facultad de Ciencias, Ciudad Universitaria, C1428 Mexico City, Ciudad de Buenos Aires, Argentina*

Kelsey A. Jackson − *College of Arts and Sciences, Creighton University, Omaha, Nebraska 68178, United States*

Mario Tagliazucchi − *INQUIMAE-CONICET and DQIAQF, Universidad de Buenos Aires, Facultad de Ciencias, Ciudad Universitaria, C1428 Mexico City, Ciudad de Buenos Aires, Argentina;* orcid.org/0000-0003-4755-955X

Samuel I. Stupp − *Department of Materials Science & Engineering, Chemistry, Biomedical Engineering, Medicine, and Simpson Querrey Institute, Northwestern University, Evanston, Illinois 60208, United States;* orcid.org/0000-0002-5491-7442

Complete contact information is available at: https://pubs.acs.org/10.1021/acs.biomac.1c00379

Author Contributions

M.C.-S. conceived the idea and supervised the research. H.X. performed synthesis (**PA-OPO$_3$H$_2$**), the CD, TEM, and AFM experiments, sample preparation, and biological assay. S.M.C. and S.R.L. performed and analyzed cryo-TEM and SAXS. V.R.U. performed synthesis (**PA-COOH**, **PA-SO$_3$H**, and **PA-OPO$_3$H$_2$**), captured images (TEM and AFM), and performed CD. M.T. (**PA-CONHSO$_2$CH$_3$**, **PA-CONHCN**, **PA-CONHSO$_2$CF$_3$**, and **PA-OPO$_3$H$_2$**) and K.A.J. (**PA-SO$_3$H**) contributed to synthesis. N.R.d.A. performed synthesis (**PA-COOH**) and CD. C.H.-I. and A.S.P. contributed to the general discussion, suggested experiments, and performed (different pH), processed, and fitted SAXS patterns. G.Z. and M.T. suggested experiments, designed the computational model, and analyzed and interpreted the results. S.I.S. contributed to the development of the project and provided access to instrumentation. All authors provided critical comments and helped with manuscript writing.

Funding

Acknowledgment is made to the donors of the American Chemical Society Petroleum Research Fund for support of this research (MC-S, Grant # 57434-DN17) and the National Science Foundation (CAREER, Award # 1941731). This project was also funded by the U.S. Department of Energy, Office of Science, Basic Energy Sciences (Award # DE-SC0000989).

Notes

The authors declare no competing financial interest.

■ ACKNOWLEDGMENTS

X-ray scattering and cryogenic TEM are supported by the Center for Bio-Inspired Energy Science, an Energy Frontier Research Center funded by the U.S. Department of Energy, Office of Science, Basic Energy Sciences under Award # DE-SC0000989. The authors are thankful to the Brazilian Synchrotron Light Laboratory (LNLS-CNPEM) for granting access to SAXS-1 Beamline (proposal SAXS-1 20190212) and the DuPont-Northwestern-Dow Collaborative Access Team (DND- CAT) located at Sector 5 of the Advanced Photon Source (APS). This research used resources of the Advanced Photon Source, a U.S. Department of Energy (DOE) Office of Science User Facility operated for the DOE Office of Science by Argonne National Laboratory under Contract no. DE-AC02-06CH11357. Special thanks to Dr. Liam C. Palmer for his assistance in reading the manuscript and for intellectual input. The authors thank Dr. Gaelle Spagnol for technical support. The authors thank the Electron Microscopy Core Facility (EMCF) and Nanoimaging Core Facility at UNMC for experimental assistance. A.S.P., C.H.-I., and M.T. are CONICET fellows. C.H.-I. acknowledges funding from ANPCyT (PICT 2017 3150). M.T. acknowledges funding from ANPCyT (PICT 2016 0154) and a CONICET−NIH International Cooperation Grant.

■ ABBREVIATIONS

PA, peptide amphiphiles; SPPS, solid-phase peptide synthesis; SAXS, small angle X-ray scattering; CD, circular dichroism; TEM, transition electron microscopy; AFM, atomic force microscopy; HPLC, high-performance liquid chromatography; MALDI, matrix-assisted laser desorption/ionization

■ REFERENCES

(1) Stephanopoulos, N.; Ortony, J. H.; Stupp, S. I. Self-Assembly for the Synthesis of Functional Biomaterials. *Acta Mater.* **2013**, *61*, 912−930.

(2) Aida, T.; Meijer, E. W.; Stupp, S. I. Functional Supramolecular Polymers. *Science* **2012**, *335*, 813−817.

(3) Whitesides, G. M.; Boncheva, M. Beyond Molecules: Self-Assembly of Mesoscopic and Macroscopic Components. *Proc. Natl. Acad. Sci. U.S.A.* **2002**, *99*, 4769−4774.

(4) Webber, M. J.; Tongers, J.; Renault, M.-A.; Roncalli, J. G.; Losordo, D. W.; Stupp, S. I. Development of Bioactive Peptide Amphiphiles for Therapeutic Cell Delivery. *Acta Biomater.* **2010**, *6*, 3−11.

(5) Soukasene, S.; Toft, D. J.; Moyer, T. J.; Lu, H.; Lee, H.-K.; Standley, S. M.; Cryns, V. L.; Stupp, S. I. Antitumor Activity of Peptide Amphiphile Nanofiber-Encapsulated Camptothecin. *ACS Nano* **2011**, *5*, 9113−9121.

(6) Matson, J. B.; Stupp, S. I. Drug Release from Hydrazone-Containing Peptide Amphiphiles. *Chem. Commun.* **2011**, *47*, 7962−7964.
(7) Rajangam, K.; Behanna, H. A.; Hui, M. J.; Han, X.; Hulvat, J. F.; Lomasney, J. W.; Stupp, S. I. Heparin Binding Nanostructures to Promote Growth of Blood Vessels. *Nano Lett.* **2006**, *6*, 2086−2090.
(8) Shah, R. N.; Shah, N. A.; Del Rosario Lim, M. M.; Hsieh, C.; Nuber, G.; Stupp, S. I. Supramolecular Design of Self-Assembling Nanofibers for Cartilage Regeneration. *Proc. Natl. Acad. Sci. U.S.A.* **2010**, *107*, 3293−3298.
(9) Mata, A.; Geng, Y.; Henrikson, K. J.; Aparicio, C.; Stock, S. R.; Satcher, R. L.; Stupp, S. I. Bone Regeneration Mediated by Biomimetic Mineralization of a Nanofiber Matrix. *Biomaterials* **2010**, *31*, 6004−6012.
(10) Standley, S. M.; Toft, D. J.; Cheng, H.; Soukasene, S.; Chen, J.; Raja, S. M.; Band, V.; Band, H.; Cryns, V. L.; Stupp, S. I. Induction of Cancer Cell Death by Self-Assembling Nanostructures Incorporating a Cytotoxic Peptide. *Cancer Res.* **2010**, *70*, 3020−3026.
(11) Toft, D. J.; Moyer, T. J.; Standley, S. M.; Ruff, Y.; Ugolkov, A.; Stupp, S. I.; Cryns, V. L. Coassembled Cytotoxic and Pegylated Peptide Amphiphiles Form Filamentous Nanostructures with Potent Anti-tumor Activity in Models of Breast Cancer. *ACS Nano* **2012**, *6*, 7956−7965.
(12) Rodrigues de Almeida, N.; Han, Y.; Perez, J.; Kirkpatrick, S.; Wang, Y.; Sheridan, M. C. Design, Synthesis, and Nanostructure-Dependent Antibacterial Activity of Cationic Peptide Amphiphiles. *ACS Appl. Mater. Interfaces* **2018**, *11*, 2790.
(13) Hartgerink, J. D.; Beniash, E.; Stupp, S. I. Self-Assembly and Mineralization of Peptide-Amphiphile Nanofibers. *Science* **2001**, *294*, 1684−1688.
(14) Dehsorkhi, A.; Castelletto, V.; Hamley, I. W. Self-assembling amphiphilic peptides. *J. Pept. Sci.* **2014**, *20*, 453−467.
(15) Löwik, D. W. P. M.; van Hest, J. C. M. Peptide Based Amphiphiles. *Chem. Soc. Rev.* **2004**, *33*, 234−245.
(16) Tantakitti, F.; Boekhoven, J.; Wang, X.; Kazantsev, R. V.; Yu, T.; Li, J.; Zhuang, E.; Zandi, R.; Ortony, J. H.; Newcomb, C. J.; Palmer, L. C.; Shekhawat, G. S.; de la Cruz, M. O.; Schatz, G. C.; Stupp, S. I. Energy Landscapes and Functions of Supramolecular Systems. *Nat. Mater.* **2016**, *15*, 469−476.
(17) Moyer, T. J.; Finbloom, J. A.; Chen, F.; Toft, D. J.; Cryns, V. L.; Stupp, S. I. pH and Amphiphilic Structure Direct Supramolecular Behavior in Biofunctional Assemblies. *J. Am. Chem. Soc.* **2014**, *136*, 14746−14752.
(18) Korevaar, P. A.; Newcomb, C. J.; Meijer, E. W.; Stupp, S. I. Pathway Selection in Peptide Amphiphile Assembly. *J. Am. Chem. Soc.* **2014**, *136*, 8540−8543.
(19) Ghosh, A.; Buettner, C. J.; Manos, A. A.; Wallace, A. J.; Tweedle, M. F.; Goldberger, J. E. Probing Peptide Amphiphile Self-Assembly in Blood Serum. *Biomacromolecules* **2014**, *15*, 4488−4494.
(20) Buettner, C. J.; Wallace, A. J.; Ok, S.; Manos, A. A.; Nicholl, M. J.; Ghosh, A.; Tweedle, M. F.; Goldberger, J. E. Balancing the Intermolecular Forces in Peptide Amphiphiles for Controlling Self-Assembly Transitions. *Org. Biomol. Chem.* **2017**, *15*, 5220−5226.
(21) Ozkan, A. D.; Tekinay, A. B.; Guler, M. O.; Tekin, E. D. Effects of Temperature, pH and Counterions on the Stability of Peptide Amphiphile Nanofiber Structures. *RSC Adv.* **2016**, *6*, 104201−104214.
(22) Toksoz, S.; Mammadov, R.; Tekinay, A. B.; Guler, M. O. Electrostatic Effects on Nanofiber Formation of Self-Assembling Peptide Amphiphiles. *J. Colloid Interface Sci.* **2011**, *356*, 131−137.
(23) Cote, Y.; Fu, I. W.; Dobson, E. T.; Goldberger, J. E.; Nguyen, H. D.; Shen, J. K. Mechanism of the pH-Controlled Self-Assembly of Nanofibers from Peptide Amphiphiles. *J. Phys. Chem. C* **2014**, *118*, 16272−16278.
(24) Zaldivar, G.; Vemulapalli, S.; Udumula, V.; Conda-Sheridan, M.; Tagliazucchi, M. Self-Assembled Nanostructures of Peptide Amphiphiles: Charge Regulation by Size Regulation. *J. Phys. Chem. C* **2019**, *123*, 17606−17615.
(25) Lin, B. F.; Marullo, R. S.; Robb, M. J.; Krogstad, D. V.; Antoni, P.; Hawker, C. J.; Campos, L. M.; Tirrell, M. V. De Novo Design of Bioactive Protein-Resembling Nanospheres via Dendrimer-Templated Peptide Amphiphile Assembly. *Nano Lett.* **2011**, *11*, 3946−3950.
(26) Andrievski, R. A. Review Stability of Nanostructured Materials. *J. Mater. Sci.* **2003**, *38*, 1367−1375.
(27) Chen, C. H.; Palmer, L. C.; Stupp, S. I. Self-Repair of Structure and Bioactivity in a Supramolecular Nanostructure. *Nano Lett.* **2018**, *18*, 6832−6841.
(28) Lassalas, P.; Gay, B.; Lasfargeas, C.; James, M. J.; Tran, V.; Vijayendran, K. G.; Brunden, K. R.; Kozlowski, M. C.; Thomas, C. J.; Smith, A. B.; Huryn, D. M.; Ballatore, C. Structure Property Relationships of Carboxylic Acid Isosteres. *J. Med. Chem.* **2016**, *59*, 3183−3203.
(29) Garvey, D. S.; Wasicak, J. T.; Elliott, R. L.; Lebold, S.; Hettinger, A.-M.; Carrera, G. M.; Lin, N.-H.; He, Y.; Holladay, M. W. Ligands for Brain Cholinergic Channel Receptors: Synthesis and in Vitro Characterization of Novel Isoxazoles and Isothiazoles as Bioisosteric Replacements for the Pyridine Ring in Nicotine. *J. Med. Chem.* **1994**, *37*, 4455−4463.
(30) Samad, M. B.; Chhonker, Y. S.; Contreras, J. I.; McCarthy, A.; McClanahan, M. M.; Murry, D. J.; Conda-Sheridan, M. Developing Polyamine-Based Peptide Amphiphiles with Tunable Morphology and Physicochemical Properties. *Macromol. Biosci.* **2017**, *17*, 1700096.
(31) Maldonado, L.; Debais, G.; Davia, F.; Méndez De Leo, L. P.; Tagliazucchi, M. Interpolymer Complexes of Poly(sulfonic acid)s and Poly(ethylene oxide): an Unexpected Association. *Soft Matter* **2019**, *15*, 9318−9324.
(32) Guthrie, J. P. Hydrolysis of Esters of Oxy Acids: pKa Values for Strong Acids; Brønsted Relationship for Attack of Water at Methyl; Free Energies of Hydrolysis of Esters of Oxy acids; and a Linear Relationship Between Free Energy of Hydrolysis and pKa Holding Over a Range of 20 pK Units. *Can. J. Chem.* **1978**, *56*, 2342−2354.
(33) Dong, H.; Du, H.; Wickramasinghe, S. R.; Qian, X. The Effects of Chemical Substitution and Polymerization on the pKa Values of Sulfonic Acids. *J. Phys. Chem. B* **2009**, *113*, 14094−14101.
(34) Rayne, S.; Forest, K. Estimated pKa Values for the Environmentally Relevant C1 Through C8 Perfluorinated Sulfonic Acid Isomers. *J. Environ. Sci. Health, Part A: Toxic/Hazard. Subst. Environ. Eng.* **2016**, *51*, 1018−1023.
(35) Powell, K. J.; Brown, P. L.; Byrne, R. H.; Gajda, T.; Hefter, G.; Sjöberg, S.; Wanner, H. Chemical Speciation of Environmentally Significant Heavy Metals with Inorganic Ligands Part 1: The Hg^{2+}- Cl^-, OH^-, CO_3^{2-}, SO_4^{2-}, and PO_4^{3-} aqueous systems. *Pure Appl. Chem.* **2005**, *77*, 739−800.
(36) Mock, W. L.; Xu, X. D. Catalytic Hydrolysis of Acylcyanamide Substrates by Carboxypeptidase A Defines the Stereochemistry of Carbonyl Hydration at the Enzyme Active Site. *Bioorg. Chem.* **1994**, *22*, 373−386.
(37) Gabor, K. A.; Stevens, C. R.; Pietraszewski, M. J.; Gould, T. J.; Shim, J.; Yoder, J. A.; Lam, S. H.; Gong, Z.; Hess, S. T.; Kim, C. H. Super Resolution Microscopy Reveals that Caveolin-1 is Required for Spatial Organization of CRFB1 and Subsequent Antiviral Signaling in Zebrafish. *PLoS One* **2013**, *8*, No. e68759.
(38) Feigin, L. A.; Svergun, D. I.; Taylor, G. W. Determination of the Integral Parameters of Particles. In *Structure Analysis by Small-Angle X-Ray and Neutron Scattering*; Feigin, L. A., Svergun, D. I., Taylor, G. W., Eds.; Springer US: Boston, MA, 1987; pp 59−105.
(39) Hammouda, B. A new Guinier−Porod model. *J. Appl. Crystallogr.* **2010**, *43*, 716−719.
(40) Pashuck, E. T.; Cui, H.; Stupp, S. I. Tuning Supramolecular Rigidity of Peptide Fibers through Molecular Structure. *J. Am. Chem. Soc.* **2010**, *132*, 6041−6046.
(41) Gao, C.; Li, H.; Li, Y.; Kewalramani, S.; Palmer, L. C.; Dravid, V. P.; Stupp, S. I.; Olvera de la Cruz, M.; Bedzyk, M. J. Electrostatic Control of Polymorphism in Charged Amphiphile Assemblies. *J. Phys. Chem. B* **2017**, *121*, 1623−1628.
(42) Mizan, T. I.; Savage, P. E.; Ziff, R. M. Temperature Dependence of Hydrogen Bonding in Supercritical Water. *J. Phys. Chem.* **1996**, *100*, 403−408.

https://doi.org/10.1021/acs.biomac.1c00379
Biomacromolecules XXXX, XXX, XXX−XXX

(43) Tang, X. C.; Pikal, M. J.; Taylor, L. S. The Effect of Temperature on Hydrogen Bonding in Crystalline and Amorphous Phases in Dihydropyrine Calcium Channel Blockers. *Pharm. Res.* **2002**, *19*, 484−490.
(44) Schneider, C. A.; Rasband, W. S.; Eliceiri, K. W. NIH Image to ImageJ: 25 years of image analysis. *Nat. Methods* **2012**, *9*, 671−675.
(45) Zhang, M.; Grossman, D.; Danino, D.; Sharon, E. Shape and Fluctuations of Frustrated Self-Assembled Nano Ribbons. *Nat. Commun.* **2019**, *10*, 3565.
(46) Ziserman, L.; Mor, A.; Harries, D.; Danino, D. Curvature Instability in a Chiral Amphiphile Self-Assembly. *Phys. Rev. Lett.* **2011**, *106*, 238105.
(47) Nakai, T.; Sugano, Y.; Shoda, M.; Sakakibara, H.; Oiwa, K.; Tuzi, S.; Imai, T.; Sugiyama, J.; Takeuchi, M.; Yamauchi, D.; Mineyuki, Y. Formation of Highly Twisted Ribbons in a Carboxymethylcellulase Gene-Disrupted Strain of a Cellulose-Producing Bacterium. *J. Bacteriol.* **2013**, *195*, 958.
(48) Zhang, L.; Wang, T.; Shen, Z.; Liu, M. Chiral Nanoarchitectonics: Towards the Design, Self-Assembly, and Function of Nanoscale Chiral Twists and Helices. *Adv. Mater.* **2016**, *28*, 1044−1059.
(49) Shimizu, T.; Masuda, M.; Minamikawa, H. Supramolecular Nanotube Architectures Based on Amphiphilic Molecules. *Chem. Rev.* **2005**, *105*, 1401−1444.
(50) Assenza, S.; Adamcik, J.; Mezzenga, R.; De Los Rios, P. Universal Behavior in the Mesoscale Properties of Amyloid Fibrils. *Phys. Rev. Lett.* **2014**, *113*, 268103.
(51) Zaldivar, G.; Conda-Sheridan, M.; Tagliazucchi, M. Twisting of Charged Nanoribbons to Helicoids Driven by Electrostatics. *J. Phys. Chem. B* **2020**, *124*, 3221−3227.
(52) Uesaka, A.; Ueda, M.; Makino, A.; Imai, T.; Sugiyama, J.; Kimura, S. Morphology Control between Twisted Ribbon, Helical Ribbon, and Nanotube Self-Assemblies with His-Containing Helical Peptides in Response to pH Change. *Langmuir* **2014**, *30*, 1022−1028.

https://doi.org/10.1021/acs.biomac.1c00379
Biomacromolecules XXXX, XXX, XXX−XXX